

Coherent structures and the saturation of a nonlinear dynamo

Erico L. Rempel^{1,†}, Abraham C.-L. Chian^{1,2,3}, Axel Brandenburg^{4,5},
Pablo R. Muñoz¹ and Shawn C. Shadden⁶

¹Institute of Aeronautical Technology (ITA), World Institute for Space Environment Research (WISER),
12228–900 São José dos Campos – SP, Brazil

²Observatoire de Paris, LESIA, CNRS, 92190 Meudon, France

³National Institute for Space Research (INPE), WISER, P.O. Box 515,
12227–010 São José dos Campos – SP, Brazil

⁴NORDITA, KTH Royal Institute of Technology and Stockholm University, Roslagstullsbacken 23,
SE 10691 Stockholm, Sweden

⁵Department of Astronomy, Stockholm University, SE 10691 Stockholm, Sweden

⁶Department of Mechanical Engineering, University of California, Berkeley, CA 94720, USA

(Received 27 October 2012; revised 24 May 2013; accepted 31 May 2013;
first published online 19 July 2013)

Eulerian and Lagrangian tools are used to detect coherent structures in the velocity and magnetic fields of a mean-field dynamo, produced by direct numerical simulations of the three-dimensional compressible magnetohydrodynamic equations with an isotropic helical forcing and moderate Reynolds number. Two distinct stages of the dynamo are studied: the kinematic stage, where a seed magnetic field undergoes exponential growth; and the saturated regime. It is shown that the Lagrangian analysis detects structures with greater detail, in addition to providing information on the chaotic mixing properties of the flow and the magnetic fields. The traditional way of detecting Lagrangian coherent structures using finite-time Lyapunov exponents is compared with a recently developed method called function M . The latter is shown to produce clearer pictures which readily permit the identification of hyperbolic regions in the magnetic field, where chaotic transport/dispersion of magnetic field lines is highly enhanced.

Key words: chaotic advection, dynamo theory, MHD turbulence

1. Introduction

The description of chaotic and turbulent flows by means of embedded coherent structures is a topic of great interest in the study of transport and mixing in fluids, since these structures act as organizing units in the flow, defining attracting and repelling directions, transport barriers and regions of high or low dispersion of passive scalars. There is no standard way of defining what a coherent structure is, but from the Eulerian point of view, they are often defined based on some measure related to vorticity. An example is the highly popular Q -criterion, first introduced by Hunt, Wray & Moin (1988) (see also Weiss 1991) to identify vortex cores based on the difference between the rate of strain and vorticity. Some other criteria define coherent

† Email address for correspondence: rempel@ita.br

structures or vortices based on local pressure minima (Jeong & Hussain 1995) or on quantities involving the eigenvalues of the gradient tensor of the velocity field (Chong, Perry & Cantwell 1990; Zhou *et al.* 1999; Chakraborty, Balachandar & Adrian 2005; Varun, Balasubramanian & Sujith 2008). From a Lagrangian point of view, coherent structures are seen as material surfaces that form the boundaries between regions of the flow with different behaviour, such as vortex surfaces. In Haller & Yuan (2000), these material surfaces are simply called Lagrangian coherent structures (LCSs) and are distinguished from other material surfaces in that an LCS exhibits locally the strongest attraction, repulsion or shearing in the flow. Repelling LCSs are responsible for generating stretching, attracting LCSs for folding, and shear LCSs for swirling and jet-type tracer patterns (Haller 2011). They are found by following trajectories of fluid particles, while computing quantities such as the maximum rate of divergence of neighbouring trajectories (Haller 2001; Shadden, Lekien & Marsden 2005) or the arclength of the trajectory (Madrid & Mancho 2009). Lagrangian tools are naturally suited for unsteady flows, since they take into account the temporal variations of the vector field, not just instantaneous snapshots. For recent lists of applications, see Peacock & Dabiri (2010) and Shadden (2011). We roughly define coherent structures for the purposes here as the objects organizing phase space transport. Specific definitions are given later in terms of the operators used to compute them.

Most works on LCSs have focused on hydrodynamic turbulence, mainly in two-dimensions. A few papers have computed LCSs for three-dimensional magnetohydrodynamic (MHD) systems in the conservative (Leoncini *et al.* 2006) and dissipative (Rempel, Chian & Brandenburg 2011, 2012) regimes. In the aforementioned dissipative cases, only velocity field (kinetic) structures were explored. Here, we expand our previous results by computing the kinetic and magnetic coherent structures in a MHD model of mean-field dynamo. Dynamo action consists in the amplification of magnetic field by the motion of an electrically conducting fluid, being the mechanism responsible for the equipartition-strength magnetic fields observed in planets and stars (Brandenburg & Subramanian 2005). Initially, a weak magnetic field \mathbf{B} undergoes an exponential growth in the ‘kinematic dynamo’ phase until \mathbf{B} is strong enough to impact the fluid velocity \mathbf{u} , and eventually the magnetic energy saturates. The saturation process is believed to be closely related to the suppression of Lagrangian chaos in the velocity field; a comparison between the chaoticity of the velocity field during the growth and saturation phases of the dynamo has been performed in previous works (Brandenburg, Klapper & Kurths 1995; Cattaneo, Hughes & Kim 1996; Zienicke, Politano & Pouquet 1998). In this paper, the emphasis is on the detection of coherent structures and the transport of passive scalars and magnetic field lines in the transition from the kinematic to the saturated phase. Eulerian structures are detected using the Q -criterion and, for the detection of LCSs, the traditional technique of finite-time Lyapunov exponents (FTLEs) is compared with the recently proposed function M (Madrid & Mancho 2009).

This paper is organized as follows. In §2 we describe the dynamo model adopted. The numerical results are presented in §3, where the Eulerian coherent structures and LCSs are computed for the velocity and magnetic fields. The conclusions are given in §4.

2. The model

The model is the prototype of an α^2 dynamo used by Brandenburg (2001), where a compressible isothermal gas is considered, with constant sound speed c_s , constant

dynamical viscosity μ , constant magnetic diffusivity η and constant magnetic permeability μ_0 . The following set of compressible MHD equations is solved

$$\partial_t \ln \rho + \mathbf{u} \cdot \nabla \ln \rho + \nabla \cdot \mathbf{u} = 0, \quad (2.1)$$

$$\partial_t \mathbf{u} + \mathbf{u} \cdot \nabla \mathbf{u} = -\nabla p / \rho + \mathbf{J} \times \mathbf{B} / \rho + (\mu / \rho) (\nabla^2 \mathbf{u} + \nabla \nabla \cdot \mathbf{u} / 3) + \mathbf{f}, \quad (2.2)$$

$$\partial_t \mathbf{A} = \mathbf{u} \times \mathbf{B} - \eta \mu_0 \mathbf{J}, \quad (2.3)$$

where ρ is the density, \mathbf{u} is the fluid velocity, \mathbf{A} is the magnetic vector potential, $\mathbf{J} = \nabla \times \mathbf{B} / \mu_0$ is the current density, p is the pressure, \mathbf{f} is an external forcing and $\nabla p / \rho = c_s^2 \nabla \ln \rho$, where $c_s^2 = \gamma p / \rho$ is assumed to be constant. Non-dimensional units are adopted by setting $k_1 = c_s = \rho_0 = \mu_0 = 1$, where $\rho_0 = \langle \rho \rangle$ is the spatial average of ρ and k_1 is the smallest wavenumber in the box, which has sides $L = 2\pi$ and periodic boundary conditions. Thus, the time unit is $(c_s k_1)^{-1}$, space is measured in units of k_1^{-1} , \mathbf{u} in units of c_s , \mathbf{B} in units of $(\mu_0 \rho_0)^{1/2} c_s$, p in units of ρ_0 and the unit of viscosity $\nu \equiv \mu / \rho_0$ and magnetic diffusivity η is c_s / k_1 . Equations (2.1)–(2.3) are solved with the PENCIL CODE (<http://pencil-code.googlecode.com>), which employs an explicit sixth-order finite differences scheme in space and a third-order Runge–Kutta scheme for time integration.

The initial conditions are $\ln \rho = 0$, $\mathbf{u} = 0$, and A is a set of normally distributed, uncorrelated random numbers with zero mean and standard deviation equal to 10^{-3} . The forcing function \mathbf{f} is given by

$$\mathbf{f}(\mathbf{x}, t) = \text{Re}\{N \mathbf{f}_k(t) \exp[i\mathbf{k}(t) \cdot \mathbf{x} + i\phi(t)]\}, \quad (2.4)$$

where $\mathbf{k}(t) = (k_x, k_y, k_z)$ is a time-dependent wavevector, $\mathbf{x} = (x, y, z)$ is position and $\phi(t)$, with $|\phi| < \pi$, is a random phase. On dimensional grounds the normalization factor is chosen to be $N = f_0 c_s (k c_s / \delta t)^{1/2}$, where f_0 is a non-dimensional factor, $k = |\mathbf{k}|$ and δt is the length of the integration time step. We focus on the case where $|\mathbf{k}|$ is around $k_f = 5$ and randomly select, at each time step, one of 350 possible vectors in $4.5 < |\mathbf{k}| < 5.5$. The operator \mathbf{f}_k is given by

$$\mathbf{f}_k = \frac{i\mathbf{k} \times (\mathbf{k} \times \mathbf{e}) - |\mathbf{k}|(\mathbf{k} \times \mathbf{e})}{k^2 \sqrt{2(1 - (\mathbf{k} \cdot \mathbf{e})^2) / k^2}}, \quad (2.5)$$

where \mathbf{e} is an arbitrary unit vector needed in order to generate a vector $\mathbf{k} \times \mathbf{e}$ that is perpendicular to \mathbf{k} . Note that $|\mathbf{f}_k|^2 = 1$ and the helicity density satisfies $\mathbf{f} \cdot \nabla \times \mathbf{f} = |\mathbf{k}| \mathbf{f}^2 > 0$, which is an important condition for the production of a mean-field dynamo (Moffatt 1978). The forcing function is delta-correlated in time, i.e. all points of \mathbf{f} are correlated at any instant in time but are different at the next time step. Following run 3 of Brandenburg (2001), the control parameters are set as $f_0 = 0.07$, $\nu = \eta = 0.002$ and the numerical resolution is 128^3 . Note that (2.5) differs from the corresponding equation of Brandenburg (2001) by a $\sqrt{2}$ factor, so that our value $f_0 = 0.07$ corresponds to $f_0 = 0.1$ in the work of Brandenburg (2001). The Kolmogorov dissipation scale for the hydrodynamical turbulence ($\mathbf{B} = \mathbf{0}$) in this case is $\eta_k = (\nu^3 / \epsilon)^{1/4} \approx 0.035$, where ϵ is the average rate of energy dissipation, which for homogeneous turbulence is $\epsilon \approx \nu \langle \omega^2 \rangle$, where $\omega = \nabla \times \mathbf{u}$ (Donzis, Yeung & Sreenivasan 2008). Since the numerical spatial grid scale is $\Delta x = 2\pi / 128 = 0.049$, we

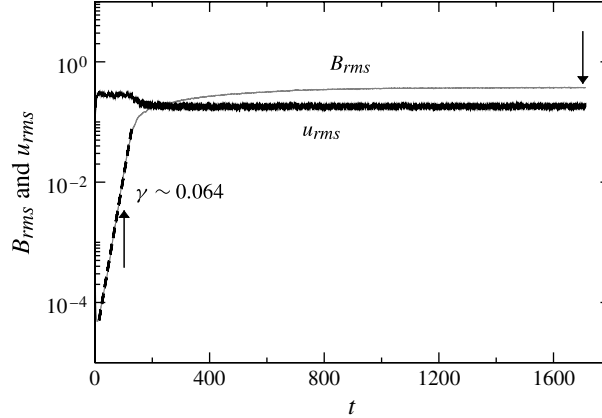


FIGURE 1. Time series of B_{rms} (light line) and u_{rms} (dark line) of MHD dynamo simulations for $\eta = \nu = 0.002$. The arrows indicate the kinematic phase at $t = 100$ and the saturated nonlinear regime at $t = 1700$, respectively. The growth rate during the kinematic phase is $\gamma \sim 0.064$.

have $\Delta x/\eta_k \approx 1.4$, which is a reasonable value, since the standard practice is to use $\Delta x/\eta_k < 2$. Therefore, the numerical resolution employed is adequate.

3. Results

3.1. Mean-field dynamo

Figure 1 shows the time series of $B_{rms} \equiv \langle B^2 \rangle^{1/2}$ (light line) and $u_{rms} \equiv \langle u^2 \rangle^{1/2}$ (dark line), where $B \equiv |\mathbf{B}|$ and $u \equiv |\mathbf{u}|$. During the first time units up to $t \sim 150$, the magnetic energy is too weak to significantly impact the velocity field and u_{rms} quickly jumps from the initial state at $u_{rms} = 0$ to $u_{rms} \sim 0.28$, thus the Reynolds number is $Re = u_{rms}/\nu k_f \sim 28$. During this ‘kinematic phase’, B_{rms} increases exponentially, with a growth rate $\gamma \sim 0.064 \pm 2 \times 10^{-5}$ obtained from the fitted line (dashed line). After $t \sim 150$, u_{rms} starts to decay due to the contribution of the Lorentz force (second term on the right-hand side of (2.2)). Eventually, the root-mean-square (r.m.s.) quantities saturate due to nonlinear effects, with $u_{rms} \sim 0.18$ while the magnetic field reaches a super-equipartition value $B_{rms} \sim 0.37 > u_{rms}$. The arrows indicate the times $t = 100$ and $t = 1700$, respectively, which will be used later to represent the kinematic and saturated phases. In turnover time units ($1/k_f u_{rms}$), the referred times are $u_{rms} k_f t \sim 140$ and $u_{rms} k_f t \sim 1530$, respectively, and the growth rate is $\gamma/u_{rms} k_f \sim 0.046$.

During the kinematic stage, the magnetic field displays low-amplitude stochastic fluctuations, as shown in figure 2(a). As B_{rms} grows, small-scale velocity and magnetic field fluctuations combine to produce a robust large-scale mean-field pattern (figure 2b). The physics behind the rise of this mean-field is related to the so-called α -effect (Moffatt 1978) and has been explored in this model by Brandenburg (2001). The α -effect generates an inverse transfer of magnetic energy, as seen in the spectra of magnetic energy depicted as dashed lines in figure 3. The solid lines represent the spectra of kinetic energy. At $t = 100$ (figure 3a) the magnetic energy is evenly spread throughout several wavenumbers around $k = 5$, with lower energy for low and high k . At $t = 1700$ (figure 3b) the magnetic energy has reached equipartition with the kinetic

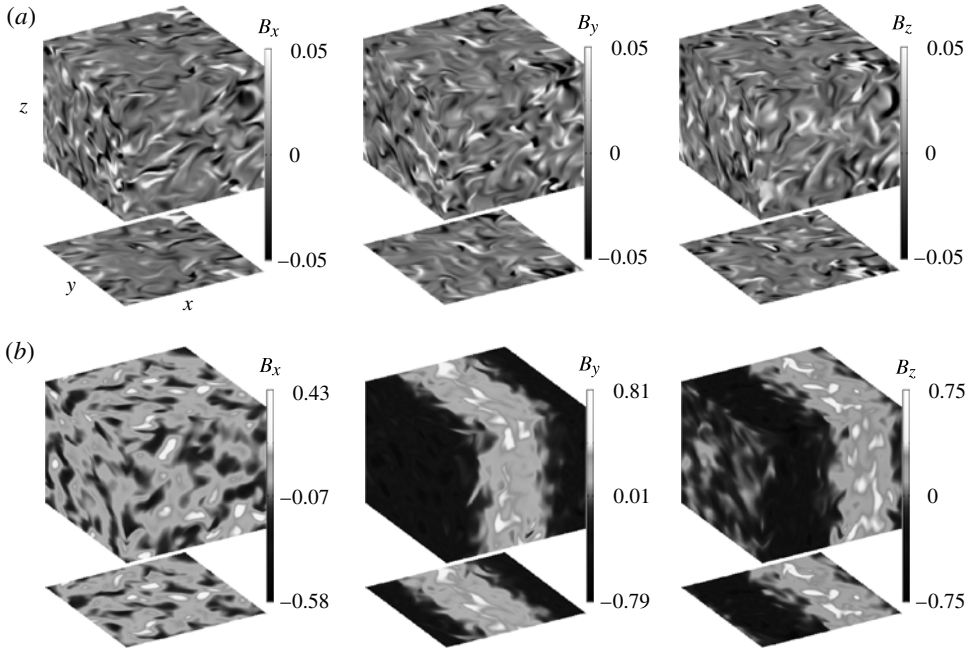


FIGURE 2. Intensity plot of magnetic field components at $t = 100$ (a) and $t = 1700$ (b).

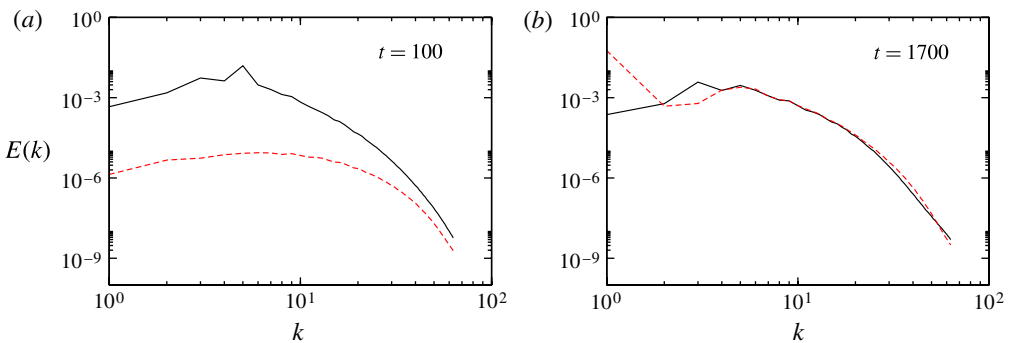


FIGURE 3. (Colour online) Spectra of magnetic (dashed lines, shown in red online) and kinetic (solid lines, shown in black) energies at times $t = 100$ (a) and $t = 1700$ (b).

energy for $k \geq 5$, but the field at the largest possible scale ($k = 1$) has much higher energy, resulting in the large-scale magnetic structures shown in figure 2(b).

3.2. Eulerian coherent structures

Eulerian coherent structures can be extracted from the velocity field by decomposing the gradient tensor $\nabla \mathbf{u}$ as

$$\nabla \mathbf{u} = \mathbf{S} + \mathbf{\Omega}, \quad (3.1)$$

where $\mathbf{S} = [\nabla \mathbf{u} + (\nabla \mathbf{u})^T]/2$ and $\mathbf{\Omega} = [\nabla \mathbf{u} - (\nabla \mathbf{u})^T]/2$ are the symmetric and antisymmetric parts of $\nabla \mathbf{u}$, respectively. The symmetric part is the rate-of-strain tensor

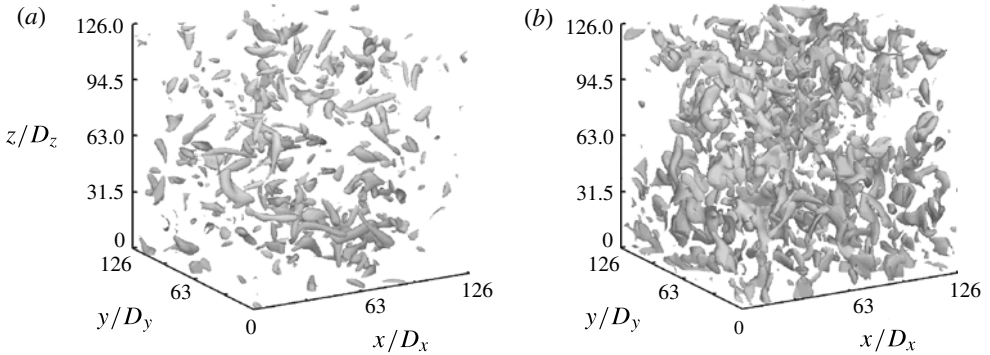


FIGURE 4. Eulerian coherent structures in the velocity field, detected by instantaneous isosurfaces of the Q -criterion. The isosurfaces are defined using 15% maximum Q : (a) $t = 100$; (b) $t = 1700$.

and the antisymmetric part is the vorticity tensor. One way to define an Eulerian coherent structure is by finding regions of \mathbf{u} where vorticity dominates over strain, which can be measured by the Q -criterion (Hunt *et al.* 1988; Zhong, Huang & Adrian 1998; Haller 2005; Lawson & Barakos 2010)

$$Q = \frac{1}{2} [|\boldsymbol{\Omega}|^2 - |\mathbf{S}|^2]. \quad (3.2)$$

Thus, an Eulerian coherent structure or vortex is defined as a region where $Q > 0$.

Figure 4 shows the isosurfaces of the Q -criterion, using 15% maximum Q (contour surfaces enclose high Q values). These plots are highly dependent on the threshold chosen for Q , but it is possible to see that the fluid is more intermittent at the kinematic dynamo phase ($t = 100$) than after saturation ($t = 1700$), since in figure 4(b) the coherent structures fill the space in a more homogeneous way. There are fewer regions for $t = 100$ where Q is much higher than the average, thus the presence of fewer vortices for this threshold in figure 4(a) than in figure 4(b), where local values of Q are closer to the average Q . Figure 5 shows the corresponding plots of Q for the magnetic field, where the coherent structures represent magnetic vortices or current structures (Brandenburg *et al.* 1996).

In figure 6, intensity plots of the Q -criterion are shown for two-dimensional slices of the box at planes $z = 0$ (a,c) and $x = 0$ (b,d) at times $t = 100$ (a,b) and $t = 1700$ (c,d), respectively. Coherent structures with strong vorticity are observed as bright spots, such as that highlighted by a box in figure 6(a). Note that at $t = 1700$ a large number of bright spots is seen in the xy -plane, but they are rare in the yz -plane, revealing a preferential alignment of coherent structures in the vertical direction in the saturated regime. A similar plot is shown for the magnetic field in figure 7, where some of the same coherent structures found in the velocity field can be observed, reflecting the strong coupling between \mathbf{B} and \mathbf{u} in (2.2) and (2.3).

Although some coherent structures are clearly detected by this Eulerian technique, the Q -criterion relies on a user defined threshold to determine their boundaries. In order to precisely identify the boundaries and the main transport barriers in the flow, the next section proceeds with a Lagrangian analysis.

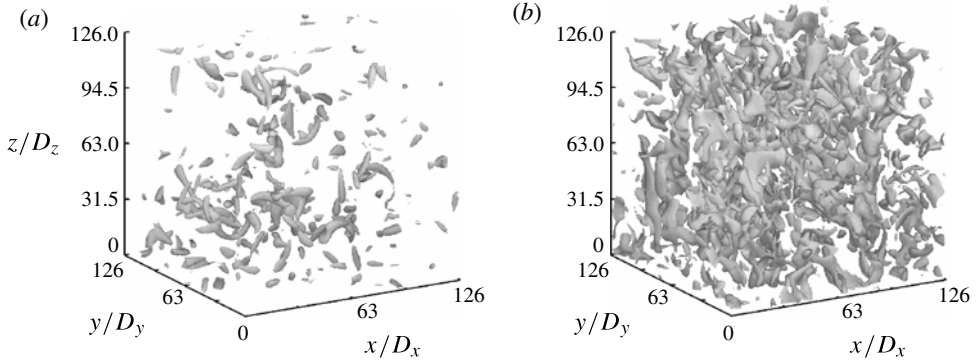


FIGURE 5. Eulerian coherent structures in the magnetic field, detected by isosurfaces of the Q -criterion. The isosurfaces are defined using 15 % maximum Q : (a) $t = 100$; (b) $t = 1700$.

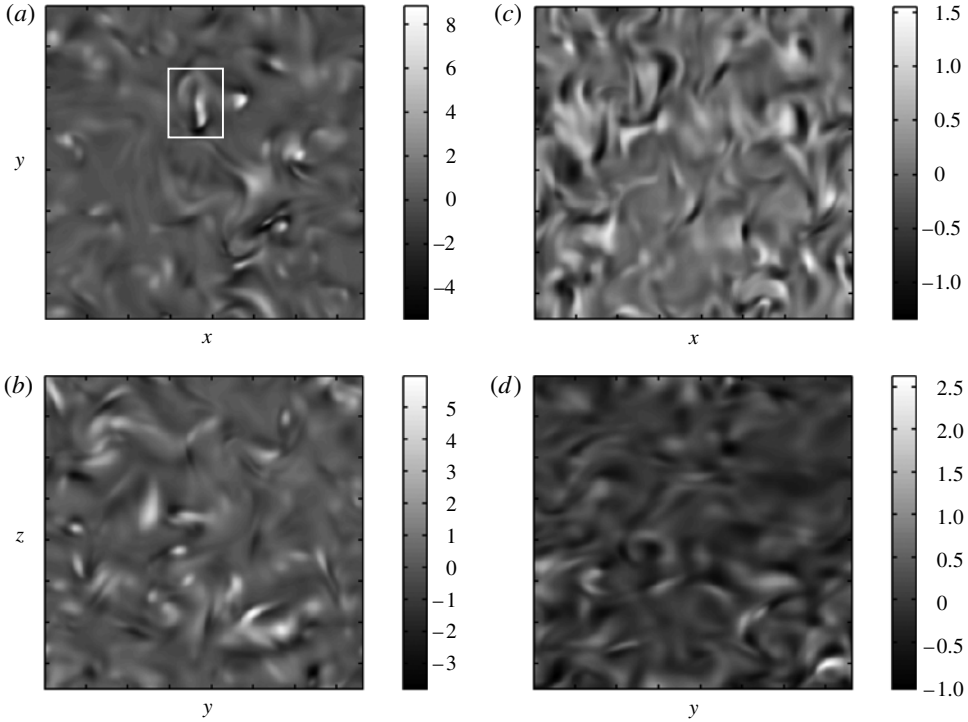


FIGURE 6. Eulerian coherent structures in the velocity field, detected by the Q -criterion at $t = 100$ (a,b) and $t = 1700$ (c,d).

3.3. LCSs

This section describes two tools that can be employed to define/detect coherent structures in the Lagrangian frame, the FTLEs and the recently proposed function M .

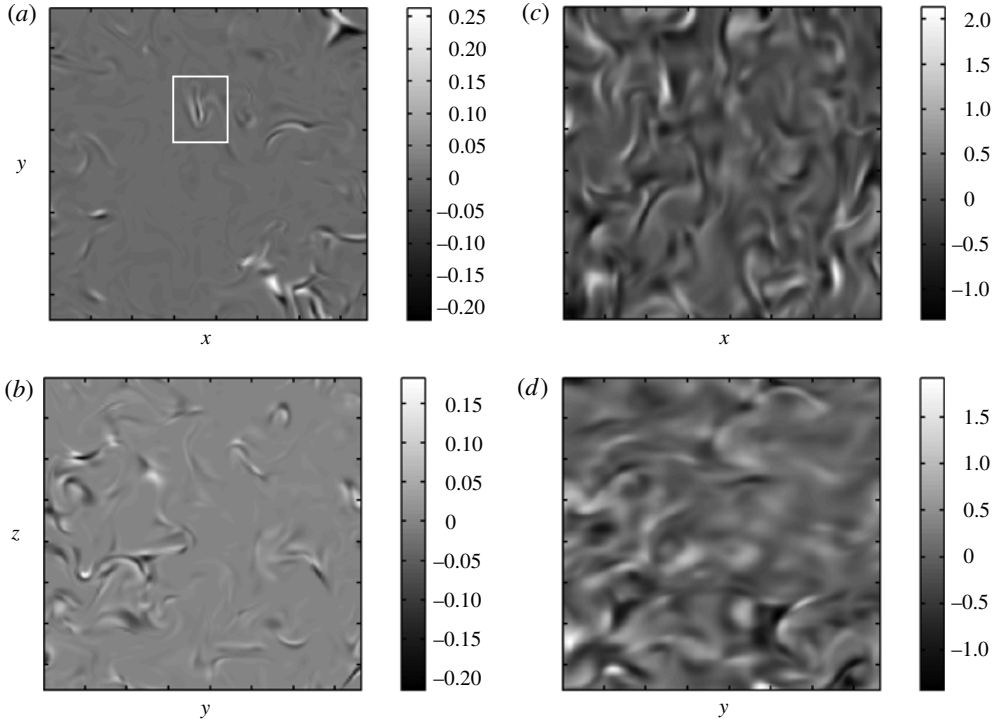


FIGURE 7. Eulerian coherent structures in the magnetic field, detected by the Q -criterion at $t = 100$ (a,b) and $t = 1700$ (c,d).

3.3.1. FTLEs

Attracting LCSs have commonly been associated with local maximizing curves (*ridges*) in the backward-time FTLE field and repelling LCSs to ridges in the forward-time FTLE field (Shadden *et al.* 2005; Green, Rowley & Haller 2007; Beron-Vera, Orlascoaga & Goni 2010). There are limitations in such a definition, as pointed out by Haller (2011) and Farazmand & Haller (2012), e.g. a ridge in the FTLE field may indicate the presence of a shear LCS or no LCS at all. Still, ridges in the FTLE fields have been employed extensively as a reasonably good approximation to the true LCSs of the flow.

Let $D \subset \mathbb{R}^3$ be the domain of the fluid to be studied, let $\mathbf{x}(t_0) \in D$ denote the position of a passive particle at time t_0 and let $\mathbf{u}(\mathbf{x}, t)$ be the velocity field defined on D . The motion of the particle is given by the solution of the initial value problem

$$\frac{d\mathbf{x}}{dt} = \mathbf{u}(\mathbf{x}(t), t), \quad \mathbf{x}(t_0) = \mathbf{x}_0. \quad (3.3)$$

Let the flow map for \mathbf{u} be defined as $\phi_{t_0}^{t_0+\tau} : \mathbf{x}(t_0) \mapsto \mathbf{x}(t_0 + \tau)$. Thus,

$$\mathbf{x}(t_0 + \tau) = \phi_{t_0}^{t_0+\tau}(\mathbf{x}_0). \quad (3.4)$$

Now, consider the evolution of the perturbed point $\hat{\mathbf{x}}(t_0) = \mathbf{x}_0 + \delta\mathbf{x}(t_0)$, where $\delta\mathbf{x}(t_0)$ is infinitesimal. After a time interval τ , this perturbation becomes

$$\hat{\mathbf{x}}(t_0 + \tau) = \phi_{t_0}^{t_0+\tau}(\mathbf{x}_0 + \delta\mathbf{x}(t_0)). \quad (3.5)$$

By taking the Taylor series expansion of the flow about point \mathbf{x}_0 one obtains

$$\hat{\mathbf{x}}(t_0 + \tau) = \phi_0^{t_0+\tau}(\mathbf{x}_0) + D\phi_0^{t_0+\tau}(\mathbf{x})\delta\mathbf{x}(t_0) + O(\|\delta\mathbf{x}(t_0)\|^2), \quad (3.6)$$

where

$$D\phi_0^{t_0+\tau}(\mathbf{x}) \equiv \frac{\partial x_i(t_0 + \tau)}{\partial x_j(t_0)} \quad (3.7)$$

is the deformation gradient, with $x_1 \equiv x$, $x_2 \equiv y$ and $x_3 \equiv z$. Using (3.6), the perturbation vector after τ time units is

$$\begin{aligned} \delta\mathbf{x}(t_0 + \tau) &= \hat{\mathbf{x}}(t_0 + \tau) - \mathbf{x}(t_0 + \tau) \\ &= \hat{\mathbf{x}}(t_0 + \tau) - \phi_0^{t_0+\tau}(\mathbf{x}_0) \\ &= D\phi_0^{t_0+\tau}(\mathbf{x})\delta\mathbf{x}(t_0) + O(\|\delta\mathbf{x}(t_0)\|^2). \end{aligned} \quad (3.8)$$

The growth of linearized perturbations is obtained by dropping the $O(\|\delta\mathbf{x}(t_0)\|^2)$ terms and using the standard Euclidean norm. The magnitude of the perturbation is given by

$$\begin{aligned} \|\delta\mathbf{x}(t_0 + \tau)\| &= \sqrt{\langle D\phi_0^{t_0+\tau}(\mathbf{x})\delta\mathbf{x}(t_0), D\phi_0^{t_0+\tau}(\mathbf{x})\delta\mathbf{x}(t_0) \rangle} \\ &= \sqrt{\langle \delta\mathbf{x}(t_0), [D\phi_0^{t_0+\tau}(\mathbf{x})]^* D\phi_0^{t_0+\tau}(\mathbf{x})\delta\mathbf{x}(t_0) \rangle} \end{aligned} \quad (3.9)$$

where $[D\phi_0^{t_0+\tau}(\mathbf{x})]^*$ denotes the adjoint (transpose) of the deformation gradient and the angle brackets denote inner product. The matrix

$$\Delta = [D\phi_0^{t_0+\tau}(\mathbf{x})]^* D\phi_0^{t_0+\tau}(\mathbf{x}) \quad (3.10)$$

is a finite-time version of the (right) Cauchy–Green deformation tensor.

The initial value problem (3.3) is solved for a Cartesian grid of initial conditions $\mathbf{x}_{i,j,k}(t_0) = (x_{i,j,k}, y_{i,j,k}, z_{i,j,k})(t_0)$ to provide final locations $\mathbf{x}_{i,j,k}(t_0 + \tau)$. Neighbouring grid points can be considered for computing a finite difference approximation of the deformation gradient. Using second-order accurate centred differences for interior points, the entries in this matrix are given as follows

$$D\phi_0^{t_0+\tau}(\mathbf{x}) = \begin{pmatrix} \frac{x_{i+1,j,k}(t_0 + \tau) - x_{i-1,j,k}(t_0 + \tau)}{x_{i+1,j,k}(t_0) - x_{i-1,j,k}(t_0)} & \frac{x_{i,j+1,k}(t_0 + \tau) - x_{i,j-1,k}(t_0 + \tau)}{y_{i,j+1,k}(t_0) - y_{i,j-1,k}(t_0)} & \frac{x_{i,j,k+1}(t_0 + \tau) - x_{i,j,k-1}(t_0 + \tau)}{z_{i,j,k+1}(t_0) - z_{i,j,k-1}(t_0)} \\ \frac{y_{i+1,j,k}(t_0 + \tau) - y_{i-1,j,k}(t_0 + \tau)}{x_{i+1,j,k}(t_0) - x_{i-1,j,k}(t_0)} & \frac{y_{i,j+1,k}(t_0 + \tau) - y_{i,j-1,k}(t_0 + \tau)}{y_{i,j+1,k}(t_0) - y_{i,j-1,k}(t_0)} & \frac{y_{i,j,k+1}(t_0 + \tau) - y_{i,j,k-1}(t_0 + \tau)}{z_{i,j,k+1}(t_0) - z_{i,j,k-1}(t_0)} \\ \frac{z_{i+1,j,k}(t_0 + \tau) - z_{i-1,j,k}(t_0 + \tau)}{x_{i+1,j,k}(t_0) - x_{i-1,j,k}(t_0)} & \frac{z_{i,j+1,k}(t_0 + \tau) - z_{i,j-1,k}(t_0 + \tau)}{y_{i,j+1,k}(t_0) - y_{i,j-1,k}(t_0)} & \frac{z_{i,j,k+1}(t_0 + \tau) - z_{i,j,k-1}(t_0 + \tau)}{z_{i,j,k+1}(t_0) - z_{i,j,k-1}(t_0)} \end{pmatrix}. \quad (3.11)$$

When $\delta\mathbf{x}(t_0)$ is aligned with one of the eigenvectors of Δ , one obtains from (3.9)

$$\|\delta\mathbf{x}(t_0 + \tau)\| = \sqrt{\lambda_i(\Delta)}\|\delta\mathbf{x}(t_0)\|, \quad i = 1, 2, 3, \quad (3.12)$$

where $\lambda_1 \geq \lambda_2 \geq \lambda_3$ are the eigenvalues of Δ . Equation (3.12) can be written as

$$\|\delta\mathbf{x}(t_0 + \tau)\| = e^{\sigma_i^{t_0+\tau}(\mathbf{x})|\tau|}\|\delta\mathbf{x}(t_0)\|, \quad i = 1, 2, 3, \quad (3.13)$$

where

$$\sigma_i^{t_0+\tau}(\mathbf{x}) = \frac{1}{|\tau|} \ln \sqrt{\lambda_i}, \quad i = 1, 2, 3 \quad (3.14)$$

are the FTLEs or direct Lyapunov exponents of the trajectory. A positive σ_1 is the signature of chaotic streamlines in the velocity field, being a measure of the stretching of fluid elements (although it also incorporates shear; Haller 2011).

3.3.2. Function M

Madrid & Mancho (2009) proposed a function to identify ‘distinguished trajectories’ (DTs) which, in aperiodic time-dependent flows, have similar topological importance as hyperbolic fixed points in stationary flows. In stationary flows, hyperbolic fixed points are responsible for particle dispersion and non-hyperbolic fixed points for particle confinement. Invariant stable and unstable manifolds of hyperbolic fixed points often behave as separatrices and divide the phase space in regions with qualitatively different behaviours. The proposed function, named ‘function M ’, can reveal both hyperbolic and non-hyperbolic flow regions of time-dependent flows. Moreover, M is also useful in detecting the stable and unstable manifolds of distinguished hyperbolic trajectories (DHTs), defined as the set of points such that trajectories passing through these points at $t = t_0$ will approach the DHTs at an exponential rate as time goes to infinity or minus infinity, respectively (Branicki, Mancho & Wiggins 2011). The stable and unstable manifolds of DHTs correspond to the repelling and attracting LCSs, respectively, as defined in the § 3.3.1.

Consider the system given by (3.3), where $\mathbf{x} = \{x_1, x_2, x_3\}$. For all initial conditions \mathbf{x}_0 in D at a given time t_0 , let us define the function $M(\mathbf{x}_0, t_0) : (D, t) \rightarrow \mathbb{R}$ as

$$M(\mathbf{x}_0, t_0)_\tau = \int_{t_0-\tau}^{t_0+\tau} \left(\sum_{i=1}^3 (\mathrm{d}x_i(t)/\mathrm{d}t)^2 \right)^{1/2} dt. \quad (3.15)$$

Thus, the function M is a measure of the arclength of the curve traced by \mathbf{x}_0 . Local minima of M represent trajectories that ‘move less’, being related either to hyperbolic or non-hyperbolic DTs. The manifolds of DHTs are also visible in the M field, since one expects a sharp distinction in the lengths of trajectory curves for particles in regions with different behaviours, separated by stable and unstable manifolds, as noted by Mendoza & Mancho (2010). The technique has been successfully applied to the detection of DTs and manifolds in oceanic (Mendoza & Mancho 2010; Mendoza, Mancho & Rio 2010) and stratospheric (de la Cámara *et al.* 2012) flows.

3.3.3. Velocity field structures and chaotic mixing

The FTLEs are computed from a series of fully three-dimensional snapshots of the velocity field taken at different times from t_0 to $t_0 + \tau$. Linear interpolation in time and third-order splines in space are used to obtain the continuous vector fields necessary to obtain the particle trajectories. Figure 8 depicts the probability density functions (p.d.f.s) of the three FTLEs at $t_0 = 100$ (a) and $t_0 = 1700$ (b) computed for 64^3 particle trajectories from (3.14) with a value of τ corresponding to 9 turnover time units, where $u_{rms} \sim 0.28$ for the kinematic phase and $u_{rms} \sim 0.18$ for the saturated regime. Therefore, $\tau = 9/(k_f u_{rms}) \sim 6.4$ time units for the kinematic phase and $\tau \sim 10$ time units for the saturated phase. One can see a clear reduction of Lagrangian chaos in the velocity field at $t_0 = 1700$, with the p.d.f. of σ_1 being shrunk and shifted to the left. There are also fewer regions with two or three positive exponents. Overall, chaotic mixing is diminished due to the growth of B_{rms} and the action of the Lorentz force. The asymmetry in the distributions is typical of heterogeneous mixing, where both regular and irregular trajectories coexist (in finite-time), which means that trajectories cannot uniformly sample the phase space (see, e.g., Beron-Vera, Ollascoaga & Goni 2010).

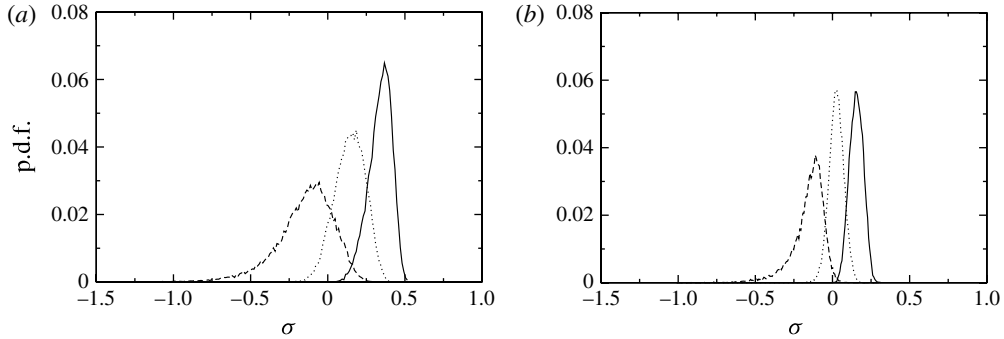


FIGURE 8. Probability density functions of the FTLEs of the velocity field at the kinematic ($t = 100$, *a*) and saturated ($t = 1700$, *b*) regimes. The solid line represents σ_1 , the dotted line, σ_2 , and the dashed line, σ_3 .

From figure 8 it is clear that most trajectories display two positive Lyapunov exponents. Zel'dovich *et al.* (1984) and Chertkov *et al.* (1999) state that in such a case, the total magnetic energy in a kinematic dynamo should behave as $B^2 \propto \exp[(\sigma_1 - \sigma_2)t]$, therefore, one has for the growth rate

$$\gamma = \frac{d \ln \langle B^2 \rangle^{1/2}}{dt} = \frac{d \ln \{ \exp[(\sigma_1 - \sigma_2)t/2] \}}{dt} = \frac{\sigma_1 - \sigma_2}{2}. \quad (3.16)$$

At $t_0 = 100$, $\langle \sigma_1 \rangle \sim 0.339$ and $\langle \sigma_2 \rangle \sim 0.143$, which from (3.16) provides $\gamma = 0.098$ (or $\gamma = 0.07$ in dimensional units), which agrees to within an order of magnitude with the fitted value $\gamma \sim 0.064$, given in figure 1.

The remainder of this paper focuses on the backward-time maximum FTLE field, since they reveal the attracting LCSs, which correspond to structures seen using flow visualization in experiments (Voth, Haller & Gollub 2002; Green *et al.* 2007). Figure 9 shows the backward-time maximum FTLE field computed for τ corresponding to 9 turnover time units at $t_0 = 100$ (*a*) and $t_0 = 1700$ (*b*) from a grid of initial conditions with 512×512 particles. The bright lines represent the attracting LCSs. While the LCSs at $t_0 = 100$ reveal no preferred direction, consistent with an isotropic forcing, at $t_0 = 1700$ there is a clear vertical alignment of LCSs in the xy -slice (figure 9*b*). This is due to the super-equipartition magnetic field at $t_0 = 1700$, which develops a large-scale vertical pattern in this plane (see figure 2), affecting the alignment of velocity field vectors.

A comparison between figures 6 and 9 shows that the FTLE field provides a clearer depiction of the objects organizing fluid transport, with finer details and more precise detection of structure boundaries. Moreover, some coherent structures are only apparent in the FTLE field, such as the large eddy indicated in figure 9(*d*).

From our experience, one of the problems with FTLE plots in turbulent flows is that pictures usually become increasingly complex for larger τ , with material lines ‘growing’ and filling the entire phase space. In that sense, it is easier to use function M to detect the main coherent structures of the flow. Figure 10 is a plot of function M with $\tau = 9$ in turnover time units, for the same velocity fields as in figure 9. Note that the M field is really showing both the attracting and repelling LCSs, since both backward and forward time integrations are performed. For the kinematic phase at $t_0 = 100$ (*a, b*) the eddies are marked by regions with strong colour distinction in

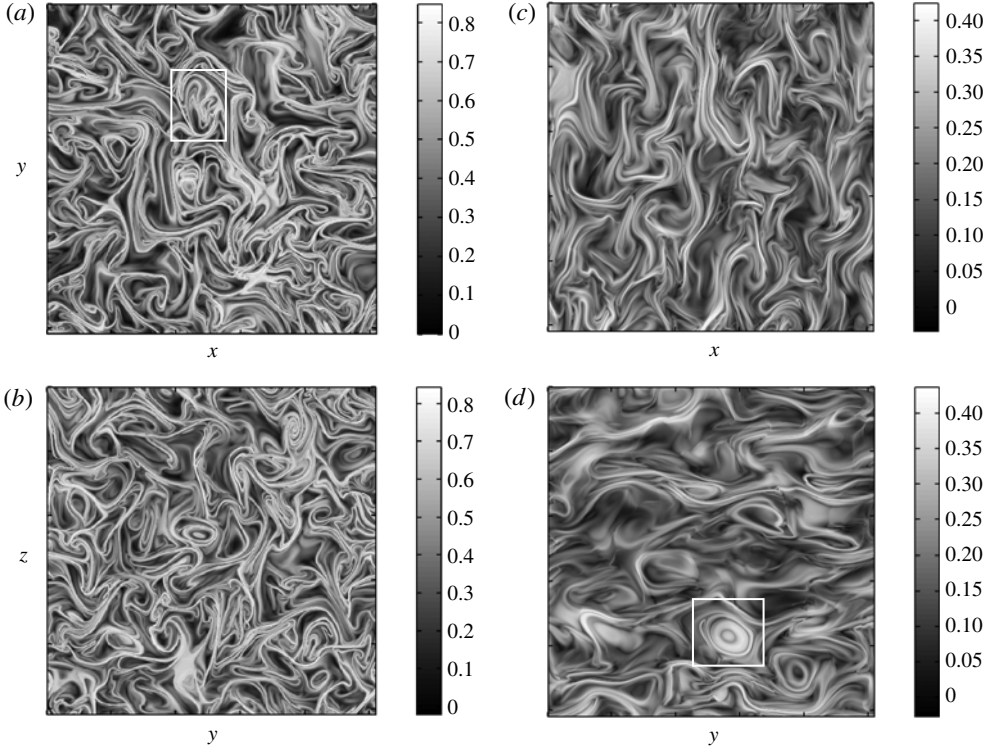


FIGURE 9. Attracting LCSs in the velocity field, given by the backward-time FTLE at $t_0 = 100$ (a,b) and $t_0 = 1700$ (c,d).

relation to their surroundings. At $t_0 = 1700$ (c,d) the borders between regions are not so sharp and there are wide smooth regions in the flow. Smoothness in the M field indicates that trajectories in those regions do not reach nearby hyperbolic regions during ± 9 turnover times, since the hyperbolic trajectories are those responsible for dispersion and for producing sharp changes in M (Mendoza & Mancho 2010). For larger τ , the boundaries become sharper and more foldings of manifolds are seen, but we keep $\tau = 9$ in all of our pictures to facilitate the comparison between both methods in different regimes. Overall, the function M seems to be less sensitive to the choice of τ than the FTLE.

3.3.4. Magnetic field structures and transport of field lines

Our simulations reveal that the magnetic field displays smooth and complex regions (see figure 7). If one applies the Lagrangian techniques discussed in the previous section to the magnetic field, the identification of magnetic LCSs provides the main barriers to the transport of field lines, a topic of great interest in magnetic reconnection studies (Evans *et al.* 2004; Grasso *et al.* 2010; Borgogno *et al.* 2011; Yeates & Hornig 2011). Another possible application is the transport of solar energetic particles perpendicular to the mean magnetic field in space plasmas, which can be explained in terms of topological trapping of field lines by magnetic islands that inhibit field line transport, and consequently particle transport (Ruffolo, Matthaeus & Chuychai 2003; Chuychai *et al.* 2005; Seripienlert *et al.* 2010).

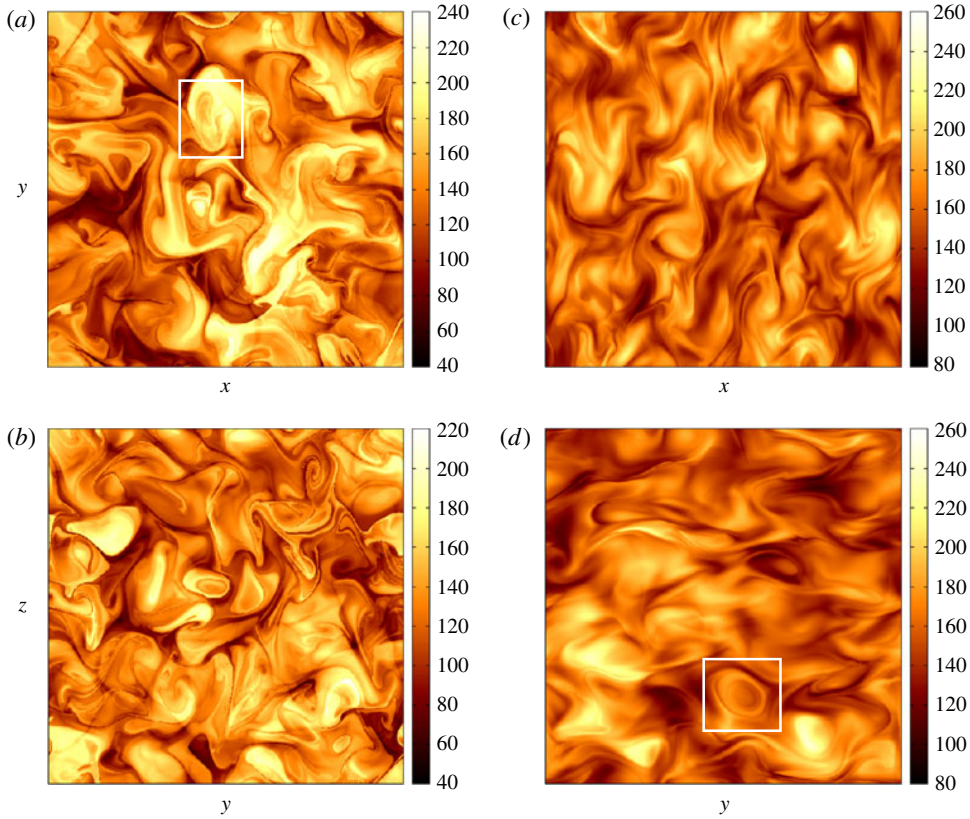


FIGURE 10. (Colour online) LCSs in the velocity field, given by the function M at $t_0 = 100$ (a,b) and $t_0 = 1700$ (c,d).

To obtain the magnetic LCSs, the magnetic field at a fixed dynamic time t_0 is used and the maximum FTLE field is computed by integrating

$$\frac{d\mathbf{x}}{ds} = \mathbf{B}(\mathbf{x}(s), t_0), \quad \mathbf{x}(s_0) = \mathbf{x}_0, \quad (3.17)$$

where the parameter (position) s along the field line is seen as an effective time, or field line time (Borgogno *et al.* 2011). The flow map for \mathbf{B} is defined as $\phi_{s_0}^{s_0+\tau} : \mathbf{x}(s_0) \rightarrow \mathbf{x}(s_0 + \tau)$. Equation (3.17) is integrated from s_0 to $s_0 + \tau$ with t fixed at t_0 . Lagrangian chaos in the magnetic field is responsible for the transport of magnetic field lines between different regions of the box. Here, the term ‘transport’ is used to refer to motion of field lines in field line time, not in dynamic time. Therefore, the maximum FTLE provides a measure of the exponential separation between two neighbouring field lines after a finite field line time τ , i.e. after a finite distance along the field line.

Figure 11 shows the backward-time maximum FTLE field for the kinematic (a) and saturated (b) regimes. The high-intensity lines represent attracting magnetic LCSs which act as barriers to field line transport. No transport of magnetic field lines occurs across invariant LCSs and large-scale transport is possible only through homoclinic and heteroclinic crossings of attracting and repelling LCSs, where a lobe dynamics

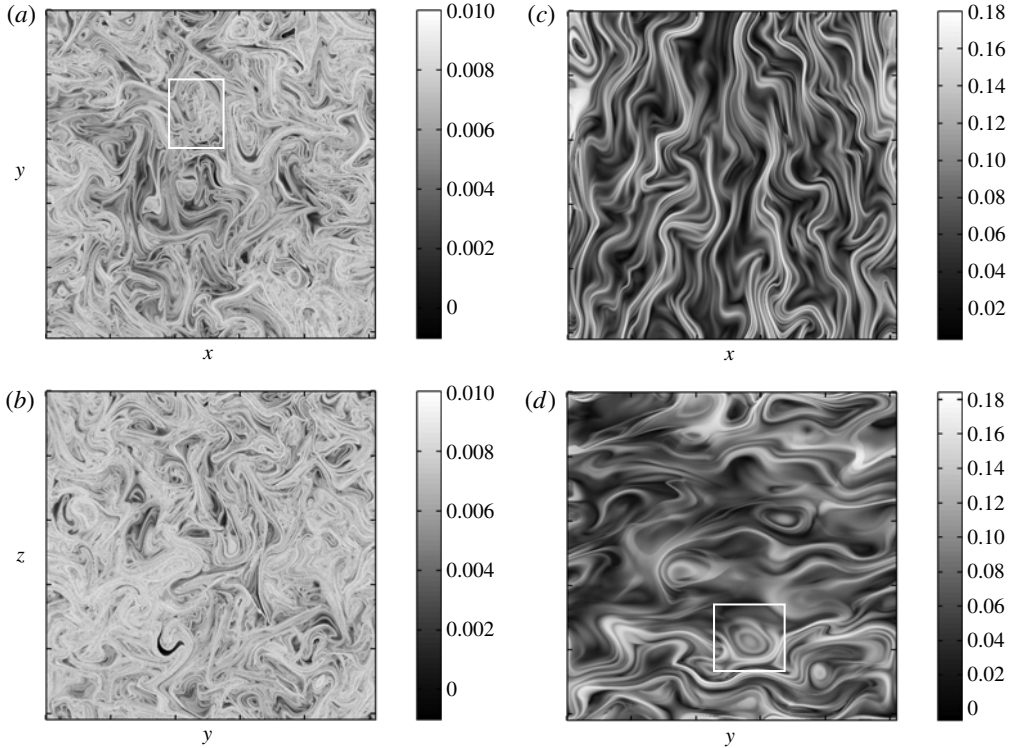


FIGURE 11. Attracting LCSs in the magnetic field, given by the backward-time maximum FTLE at $t = 100$ (*a,b*) and $t = 1700$ (*c,d*).

mechanism takes place (Grasso *et al.* 2010; Borgogno *et al.* 2011; Yeates & Hornig 2011; Rempel *et al.* 2012). Numerically, when LCSs are computed from an FTLE field, Shadden *et al.* (2005) showed that in most cases maximizing curves are advected as material surfaces. Under appropriate conditions (Haller 2011) this can break down for the FTLE measure, but these conditions are not typically encountered in conservative flows. Both FTLE fields are obtained by fixing the evolution (dynamic) time ($t_0 = 100$ for (*a,b*) and $t_0 = 1700$ for (*c,d*)) and setting $\tau = 9/B_{rms}$, where $B_{rms} = 0.014$ for $t_0 = 100$ and $B_{rms} = 0.37$ for $t_0 = 1700$. In the kinematic regime ($t_0 = 100$) the LCSs display no preferred direction, and randomly fill the simulation box. Note that, at least for this value of τ , it is difficult to identify the coherent structure marked in the box in figure 11(*a*) due to the many foldings of attracting lines. After growth and saturation of B_{rms} ($t_0 = 1700$), the randomness of field line orientation is diminished and there is a preferential direction of alignment of field lines which, as mentioned before, directly affects the velocity field.

Once again, to obtain a clearer picture of magnetic coherent structures, we plot in figure 12 the function M for $\tau = 9/B_{rms}$. It is easier to spot coherent structures from this field, such as that in the box in figure 12(*a*). Function M seems to be better than the FTLE field in highlighting the main coherent structures, filtering out spurious lines that are not so important for mixing (Mendoza & Mancho 2010). Nevertheless, the M function does not automatically detect the transport barriers, and one has to rely on thresholds to extract the boundaries between regions.

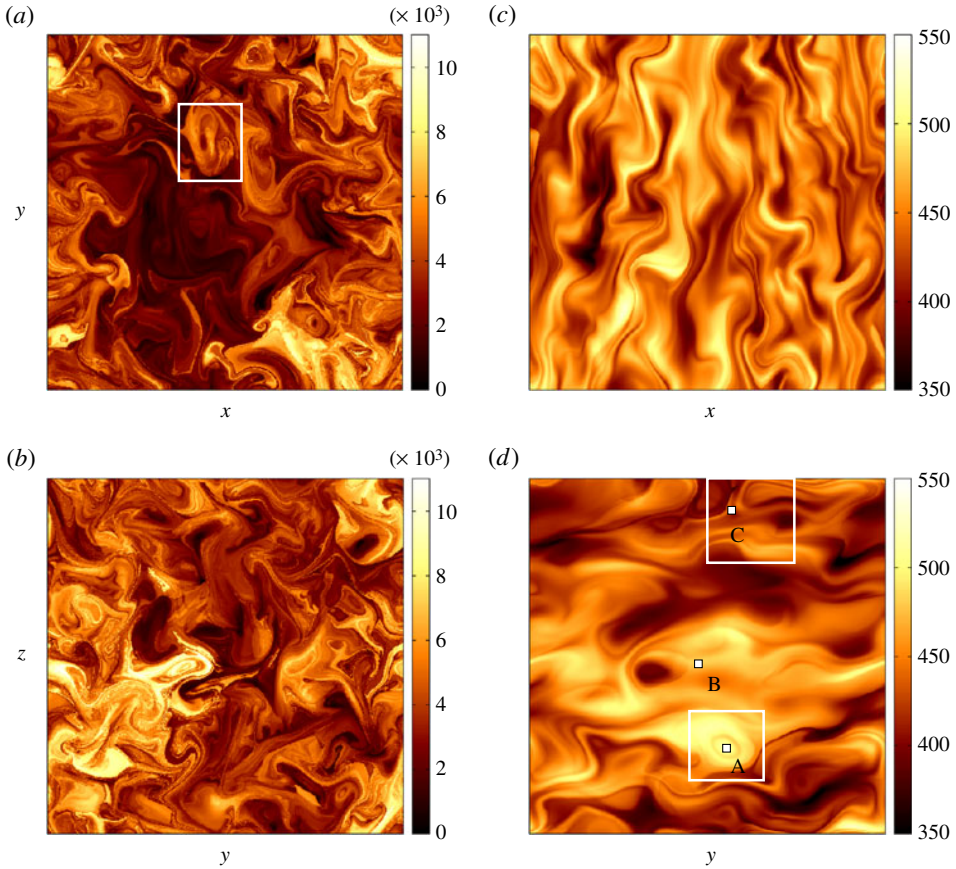


FIGURE 12. (Colour online) LCSs in the magnetic field, given by the function M at $t = 100$ (a,b) and $t = 1700$ (c,d).

As mentioned before, another feature of function M plots is that they provide both the stable and unstable manifolds of DHTs in the same picture. In order to illustrate this feature, three distinct regions are marked in figure 12(d). Regions A and B are located in smooth parts of the M field and region C in a region where manifolds are crossing. Smoothness of M in regions A and B indicates that initial conditions in these regions do not perceive nearby hyperbolic regions for $t \in (t_0 - \tau, t_0 + \tau)$ (Mendoza & Mancho 2010). An enlargement of region C is shown in figure 13, where the presence of manifolds indicates that field lines in this region either were dispersed in $t_0 - \tau$ or will disperse in $t_0 + \tau$. We define three sets of initial conditions inside the small white squares A, B and C in figure 12(d), with each square containing 25 initial conditions. The result of integrating (3.17) with each set of initial conditions for $\tau = 9/B_{rms}$ field-line-time units is shown in figure 14. Figure 14(a,b) show the trajectories of initial conditions in regions A and B, respectively, where it can be seen that all magnetic field lines stay close to each other, forming a magnetic flux tube that is not dispersed in this field line time interval. The apparent discontinuities in field lines are due to the periodic boundary conditions. In figure 14(c) the trajectories of initial conditions at region C are shown and one can see that there is great chaotic dispersion of field lines due to the crossings of manifolds in this region.

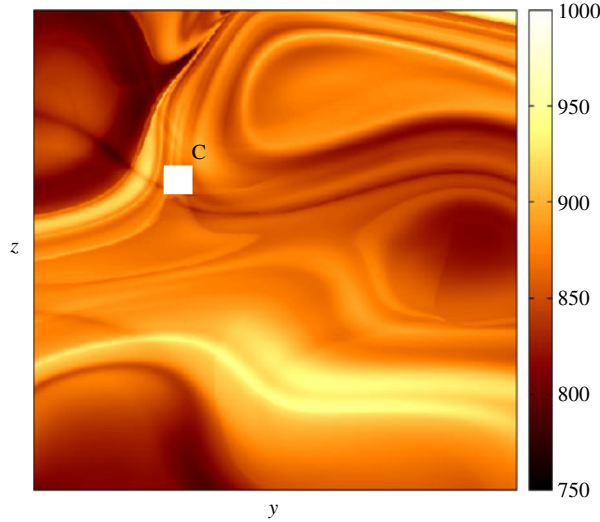


FIGURE 13. (Colour online) Enlargement of the upper rectangle in figure 12(d).

We conclude that function M can efficiently detect strong dispersion regions in a magnetic field.

3.3.5. Statistical analysis

A quantitative comparison between the statistical distributions for the velocity and magnetic fields at the kinematic and saturated dynamo regimes is shown in table 1. The statistics are computed for 128^3 initial conditions uniformly spread in the box. Table 1 shows the mean values for the Q -criterion, $\langle Q \rangle$, the backward-time FTLE, $\langle \sigma_1^{t_0-1} \rangle$, as well as the kurtosis of the M function distribution, defined as

$$K(M) = \frac{1}{N} \sum_{i=1}^N \left(\frac{M_i - \langle M \rangle}{\sigma_M} \right)^4 - 3, \quad (3.18)$$

where N is the number of grid points and σ_M is the standard deviation of M . A Gaussian distribution has $K = 0$, $K < 0$ represents a distribution with weaker tails than Gaussian (platykurtic) and $K > 0$ a distribution with stronger tails (leptokurtic). One can see that there is an increase of $\langle Q \rangle$ from $t = 100$ to $t = 1700$ for both the velocity and magnetic fields. This reflects the increase in the number of (instantaneous) Eulerian coherent structures after the dynamo saturation, as seen in figures 4 and 5. The statistics of LCSs, on the other hand, reflect a contrast between the velocity and magnetic field structures when time is taken into account, which is not seen in the Eulerian statistics. The dynamo saturation leads to a decrease in $\langle \sigma_1^{t_0-1} \rangle$ for the velocity field accompanied by an increase in $\langle \sigma_1^{t_0-1} \rangle$ for the magnetic field, which coincides with the loss of kinetic energy and gain of magnetic energy in the system. The value of $K(M)$ provides a measure of the intermittency in the spatial distribution of LCS in the M function plots, where a leptokurtic distribution implies greater intermittency. For the velocity field, the distribution of M switches from platykurtic at $t_0 = 100$ to leptokurtic at $t_0 = 1700$, whereas for the magnetic field it switches from leptokurtic ($t = 100$) to platykurtic ($t = 1700$). Thus, $K(M)$ can clearly quantify the

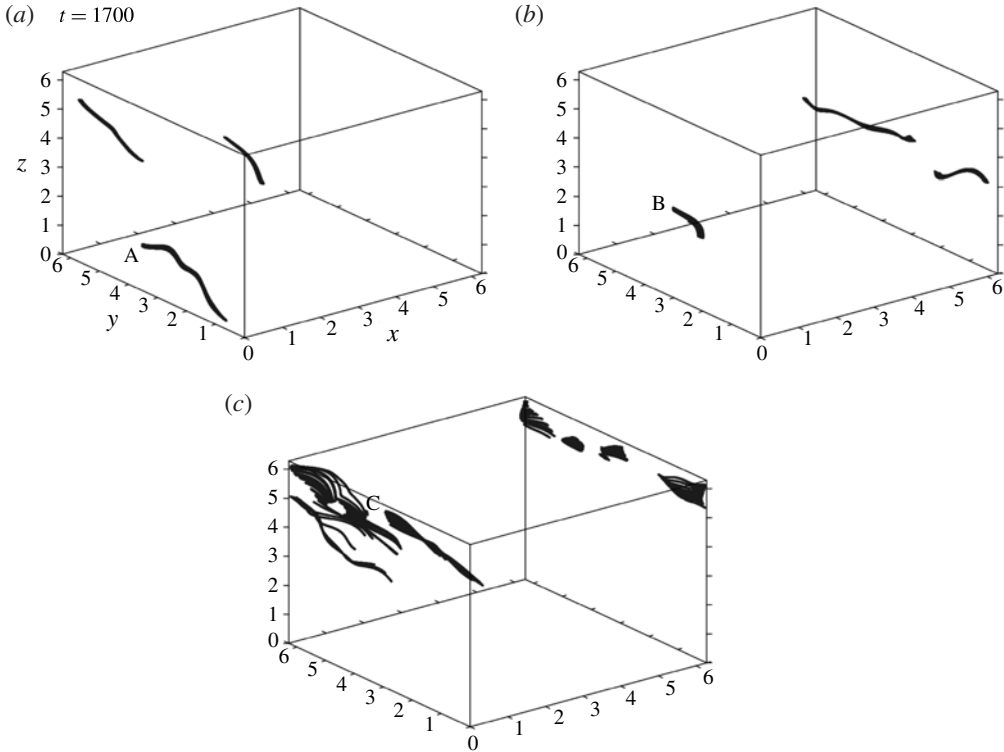


FIGURE 14. Magnetic field lines produced by advecting a small blob of initial conditions in the magnetic field at $t = 1700$: (a) the initial blob is located at A, the point inside a magnetic vortex in figure 12(d); (b) the initial blob is located at B, the point in a smooth region of figure 12(d); (c) the initial blob is located at C, the point at a crossing of manifolds in figure 12(d).

Statistics for \mathbf{u}	$\langle Q \rangle$	$\langle \sigma_1^{t_0-1} \rangle$	$K(M)$
$t = 100$	-0.0224	0.989	-0.138
$t = 1700$	-0.0109	0.592	0.458
Statistics for \mathbf{B}	$\langle Q \rangle$	$\langle \sigma_1^{t_0-1} \rangle$	$K(M)$
$t = 100$	-0.0237	0.024	4.61
$t = 1700$	4.05×10^{-5}	0.22	-0.12

TABLE 1. Statistical quantities for the velocity and magnetic fields.

difference between the kinematic and saturated dynamo phases from an LCS point of view.

4. Conclusions

MHD coherent structures have been identified in direct numerical simulations of a nonlinear dynamo. It was shown that both Eulerian and Lagrangian tools are able to extract vortices from velocity and magnetic field data. Although the Eulerian tool

adopted is less computationally expensive, Lagrangian plots show finer details and can better locate the boundaries of vortices. In addition, the Lagrangian analysis provides important information about the mixing properties of the flow. Regarding the numerical tools employed to detect LCSs, the function M seems to be less sensitive to the choice of the integration time τ in comparison with the maximum FTLE. Thus, pictures obtained with the FTLE can become increasingly ‘noisy’ with increasing τ due to the complex folding of material lines. Although function M provides ‘cleaner’ pictures, the manifolds (transport barriers) are often not as clearly traced as in a FTLE field, so we suggest the use of both tools. In future works, we plan to compare them with the recently developed technique based on the variational theory of hyperbolic LCSs (Farazmand & Haller 2012; Haller & Beron-Vera 2012).

Both tools reveal the strong impact of the magnetic field on the mixing properties of the velocity field when the system moves from the kinematic to the saturated dynamo phase. After the appearance of a strong mean field, the kinetic and magnetic coherent structures are shown to align in a preferred direction, revealing the anisotropy developed in the vector fields. Function M is also shown to be useful to detect manifolds of hyperbolic trajectories in the magnetic field, where intense transport of magnetic field lines takes place, a feature that can be further explored to study magnetic reconnection phenomena in plasmas. In relation to this, LCSs in photospheric velocity fields have been shown to be associated with quasi-separatrix layers in the magnetic field (Yeates, Hornig & Welsch 2012), which are regions of strong gradients in stretching and squashing of magnetic flux tubes, being identified as the preferential regions for magnetic reconnection (Démoulin 2006; Santos *et al.* 2008). Magnetic reconnection is an important phenomenon in nonlinear dynamos, since it is believed that it can reduce the backreaction of the Lorentz force on the velocity field (Blackman 1996). Essentially, turbulent motions can cause the stretching, twisting and folding of weak magnetic field lines in such a way as to produce the growth of magnetic flux. After the magnetic field reaches equipartition with the velocity field, the field lines can restrict fluid motions and transport of material is significantly reduced. This suppression of motions may also inhibit the dynamo. However, if there is rapid reconnection between magnetic flux tubes, this could prevent the tube from backreacting. Rapid reconnection can naturally occur in MHD turbulence, where a broad range of reconnection rates can be found, as shown by (Servidio *et al.* 2010) in the context of two-dimensional MHD turbulence by measuring the electric field at hyperbolic X -points. For other works on the role of magnetic reconnection in dynamo models, see Archontis, Dorch & Nordlund (2003) and Baggaley *et al.* (2009).

Acknowledgements

We acknowledge Professor R. A. Miranda, of the University of Brasilia, for his support with numerical codes. E.L.R. acknowledges the support of FAPESP (Brazil), CNPq (Brazil) and NORDITA (Sweden). A.C.-L.C. acknowledges support from CNPq (Brazil), the award of a Marie Curie International Incoming Fellowship and the hospitality of Paris Observatory. A.B. acknowledges the European Research Council under the AstroDyn Research Project No. 227952 and the Swedish Research Council under the project grants 621-2011-5076 and 2012-5797. P.R.M. acknowledges support from FAPESP (Brazil). S.C.S. acknowledges support from the NSF (award no. 1047963).

REFERENCES

- ARCHONTIS, V., DORCH, S. B. F. & NORDLUND, A. 2003 Numerical simulations of kinematic dynamo action. *Astron. Astrophys.* **397**, 393–399.
- BAGGLEY, A. W., BARENGHI, C. F., SHUKUROV, A. & SUBRAMANIAN, K. 2009 Reconnecting flux-rope dynamo. *Phys. Rev. E* **80**, 055301.
- BERON-VERA, F. J., OLASCOAGA, M. J. & GONI, G. J. 2010 Surface ocean mixing inferred from different multisatellite altimetry measurements. *J. Phys. Oceanogr.* **40**, 2466–2480.
- BLACKMAN, E. G. 1996 Overcoming the backreaction on turbulent motions in the presence of magnetic fields. *Phys. Rev. Lett.* **77**, 2694–2697.
- BORGOGNO, D., GRASSO, D., PEGORARO, F. & SCHEP, T. J. 2011 Barriers in the transition to global chaos in collisionless magnetic reconnection. I. Ridges on the finite time Lyapunov exponent field. *Phys. Plasmas* **18**, 102307.
- BRANDENBURG, A. 2001 The inverse cascade and nonlinear alpha-effect in simulations of isotropic helical hydromagnetic turbulence. *Astrophys. J.* **550**, 824–840.
- BRANDENBURG, A., JENNINGS, R. L., NORDLUND, A., RIEUTORD, M., STEIN, R. F. & TUOMINEN, I. 1996 Magnetic structures in a dynamo simulation. *J. Fluid Mech.* **306**, 325–352.
- BRANDENBURG, A., KLAPPER, I. & KURTHS, J. 1995 Generalized entropies in a turbulent dynamo simulation. *Phys. Rev. E* **52**, R4602–R4605.
- BRANDENBURG, A. & SUBRAMANIAN, K. 2005 Astrophysical magnetic fields and nonlinear dynamo theory. *Phys. Rep.* **417**, 1–209.
- BRANICKI, M., MANCHO, A. M. & WIGGINS, S. 2011 A Lagrangian description of transport associated with a fronteddy interaction: application to data from the North-Western Mediterranean Sea. *Physica D* **240**, 282–304.
- CATTANEO, F., HUGHES, D. W. & KIM, E.-J. 1996 Suppression of chaos in a simplified nonlinear dynamo model. *Phys. Rev. Lett.* **76**, 2057–2060.
- DE LA CÁMARA, A., MANCHO, A. M., IDE, K., SERRANO, E. & MECHOSO, C. R. 2012 Routes of transport across the Antarctic polar vortex in the southern spring. *J. Atmos. Sci.* **69**, 741–752.
- CHAKRABORTY, P., BALACHANDAR, S. & ADRIAN, R. J. 2005 On the relationships between local vortex identification schemes. *J. Fluid Mech.* **535**, 189–214.
- CHERTKOV, M., FALKOVICH, G., KOLOKOLOV, I. & VERGASSOLA, M. 1999 Small-scale turbulent dynamo. *Phys. Rev. Lett.* **83**, 4065–4068.
- CHONG, M. S., PERRY, A. E. & CANTWELL, B. J. 1990 A general classification of three-dimensional flow fields. *Phys. Fluids A* **2**, 765–777.
- CHUYCHAI, P., RUFFOLO, D., MATTHAEUS, W. H. & ROWLANDS, G. 2005 Suppressed diffusive escape of topologically trapped magnetic field lines. *Astrophys. J.* **633**, L49–L52.
- DÉMOULIN, P. 2006 Extending the concept of separatrices to QSLs for magnetic reconnection. *Adv. Space Res.* **37**, 1269–1282.
- DONZIS, D. A., YEUNG, P. K. & SREENIVASAN, K. R. 2008 Dissipation and enstrophy in isotropic turbulence: resolution effects and scaling in direct numerical simulations. *Phys. Fluids* **20**, 045108.
- EVANS, T. E., ROEDER, R. K. W., CARTER, J. A. & RAPOPORT, B. I. 2004 Homoclinic tangles, bifurcations and edge stochasticity in diverted tokamaks. *Contrib. Plasma Phys.* **44**, 235–240.
- FARAZMAND, M. & HALLER, G. 2012 Computing Lagrangian coherent structures from their variational theory. *Chaos* **22**, 013128.
- GRASSO, D., BORGOGNO, D., PEGORARO, F. & SCHEP, T. J. 2010 Barriers to old line transport in 3D magnetic configurations. *J. Phys.: Conf. Ser.* **260**, 012012.
- GREEN, M. A., ROWLEY, C. W. & HALLER, G. 2007 Detection of Lagrangian coherent structures in three-dimensional turbulence. *J. Fluid Mech.* **572**, 111–120.
- HALLER, G. 2001 Distinguished material surfaces and coherent structures in three-dimensional fluid flows. *Physica D* **149**, 248–277.
- HALLER, G. 2005 An objective definition of a vortex. *J. Fluid Mech.* **525**, 1–26.

- HALLER, G. 2011 A variational theory of hyperbolic Lagrangian coherent structures. *Physica D* **240**, 574–598.
- HALLER, G. & BERON-VERA, F. J. 2012 Geodesic theory of transport barriers in two-dimensional flows. *Physica D* **241**, 1680–1702.
- HALLER, G. & YUAN, G. 2000 Lagrangian coherent structures and mixing in two-dimensional turbulence. *Physica D* **147**, 352–370.
- HUNT, J. C. R., WRAY, A. A. & MOIN, P. 1988 Eddies, streams, and convergence zones in turbulent flows. *Center for Turbulence Research Report CTR-S88*, <http://ctr.stanford.edu/Summer/201306111537.pdf>.
- JEONG, J. & HUSSAIN, F. 1995 On the identification of a vortex. *J. Fluid Mech.* **285**, 69–94.
- LAWSON, S. J. & BARAKOS, G. N. 2010 Computational fluid dynamics analyses of flow over weapons-bay geometries. *J. Aircraft* **47**, 1605–1623.
- LEONCINI, X., AGULLO, O., MURAGLIA, M. & CHANDRE, C. 2006 From chaos of lines to Lagrangian structures in flux conservative fields. *Eur. Phys. J. B* **53**, 351–360.
- MADRID, J. A. J. & MANCHO, A. M. 2009 Distinguished trajectories in time dependent vector fields. *Chaos* **19**, 013111.
- MENDOZA, C. & MANCHO, A. M. 2010 Hidden geometry of ocean flows. *Phys. Rev. Lett.* **105**, 038501.
- MENDOZA, C., MANCHO, A. M. & RIO, M.-H. 2010 The turnstile mechanism across the Kuroshio current: analysis of dynamics in altimeter velocity fields. *Nonlinear Process. Geophys.* **17**, 103–111.
- MOFFATT, H. K. 1978 *Magnetic Field Generation in Electrically Conducting Fluids*. Cambridge University Press.
- PEACOCK, T. & DABIRI, J. 2010 Introduction to focus issue: Lagrangian coherent structures. *Chaos* **20**, 017501.
- REMPEL, E. L., CHIAN, A. C.-L. & BRANDENBURG, A. 2011 Lagrangian coherent structures in nonlinear dynamos. *Astrophys. J. Lett.* **735**, L9 (7pp).
- REMPEL, E. L., CHIAN, A. C.-L. & BRANDENBURG, A. 2012 Lagrangian chaos in an ABC-forced nonlinear dynamo. *Phys. Scr.* **86**, 018405.
- RUFFOLO, D., MATTHAEUS, W. H. & CHUYCHAI, P. 2003 Trapping of solar energetic particles by the small-scale topology of solar wind turbulence. *Astrophys. J.* **597**, L169–L172.
- SANTOS, J. C., BÜCHNER, J., MADJARSKA, M. S. & ALVES, M. V. 2008 On the relation between DC current locations and an EUV bright point: a case study. *Astron. Astrophys.* **490**, 345–352.
- SERIPIENLERT, A., RUFFOLO, D., MATTHAEUS, W. H. & CHUYCHAI, P. 2010 Dropouts in solar energetic particles: associated with local trapping boundaries or current sheets? *Astrophys. J.* **711**, 980–989.
- SERVIDIO, S., MATTHAEUS, W. H., SHAY, M. A., DMITRUK, P., CASSAK, P. A. & WAN, M. 2010 Statistics of magnetic reconnection in two-dimensional magnetohydrodynamic turbulence. *Phys. Plasmas* **17**, 032315.
- SHADDEN, S. C. 2011 Lagrangian coherent structures. In *Transport and Mixing in Laminar Flows*, pp. 59–89. Wiley-VCH Verlag GmbH & Co. KGaA.
- SHADDEN, S. C., LEKIEN, F. & MARSDEN, J. E. 2005 Definition and properties of Lagrangian coherent structures from finite-time Lyapunov exponents in two-dimensional aperiodic flows. *Physica D* **212**, 271–304.
- VARUN, A. V., BALASUBRAMANIAN, K. & SUJITH, R. I. 2008 An automated vortex detection scheme using the wavelet transform of the d_2 field. *Exp. Fluids* **45**, 857–868.
- VOTH, G. A., HALLER, G. & GOLLUB, J. P. 2002 Experimental measurements of stretching fields in fluid mixing. *Phys. Rev. Lett.* **88**, 254501.
- WEISS, J. 1991 The dynamics of enstrophy transfer in two-dimensional hydrodynamics. *Physica D* **48**, 273–294.
- YEATES, A. R. & HORNIG, G. 2011 A generalized flux function for three-dimensional magnetic reconnection. *Phys. Plasmas* **18**, 102118.
- YEATES, A. R., HORNIG, G. & WELSCH, B. T. 2012 Lagrangian coherent structures in photospheric flows and their implications for coronal magnetic structures. *Astron. Astrophys.* **539**, A1 (9pp).

- ZEL'DOVICH, YA. B., RUZMAIKIN, A. A., MOLCHANOV, S. A. & SOKOLOFF, D. D. 1984 Kinematic dynamo problem in a linear velocity field. *J. Fluid Mech.* **144**, 1–11.
- ZHONG, J., HUANG, T. S. & ADRIAN, R. J. 1998 Extracting 3D vortices in turbulent fluid flow. *IEEE Trans. Pattern Anal. Mach. Intell.* **20**, 193–199.
- ZHOU, J., ADRIAN, R. J., BALACHANDAR, S. & KENDALL, T. M. 1999 Mechanisms for generating coherent packets of hairpin vortices in channel flow. *J. Fluid Mech.* **387**, 353–396.
- ZIENICKE, E., POLITANO, H. & POUQUET, A. 1998 Variable intensity of Lagrangian chaos in the nonlinear dynamo problem. *Phys. Rev. Lett.* **81**, 4640–4643.